Discrete fracture in quasi-brittle materials under compressive and tensile stress states

P.A. Klerck [a], E.J. Sellers [b], D.R.J. Owen [a,*]

[a] *Department of Civil Engineering, University of Wales, Singleton Park, Swansea, Wales SA2 8PP, United Kingdom*
[b] *Division of Mining Technology, CSIR, Johannesburg, South Africa*

Abstract

A method for modelling discrete fracture in geomaterials under tensile and compressive stress fields has been developed based on a Mohr–Coulomb failure surface in compression and three independent anisotropic rotating crack models in tension. Extension fracturing is modelled by coupling the softening of the anisotropic rotating crack failure criterion to the compressive plastic strain evolution. Modifications were introduced into an explicit discrete element/finite element code with an explicit Lagrangian contact algorithm to enforce non-penetration of the surfaces created when the tensile strength is depleted. The model is applied to triaxial and plane strain tests, as well as punch tests and borehole breakouts to show that the model is able to quantitatively predict the appropriate load–displacement response of the system in addition to the observed evolution of discrete fracturing in situations comprising a variety of compressive and tensile stress states.
© 2004 Elsevier B.V. All rights reserved.

1. Introduction

In the analysis of the stability of mine excavations, it is vital to be able to determine the degree of fracturing in the rock and the response of the fractured rock mass to subsequent changes of the stress state, for a variety of excavation shapes and sequences. The constitutive relationship for quasi-brittle materials in compression is generally determined by performing conventional triaxial tests ($\sigma_1 = \sigma_2 \geqslant \sigma_3$), extension tests ($\sigma_1 \geqslant \sigma_2 = \sigma_3$) and true triaxial tests ($\sigma_1 \geqslant \sigma_2 \geqslant \sigma_3$) on small material specimens. Typical experimental results for rock in compression are presented and discussed by Hallbauer et al. [1], Tapponnier and Brace [2], Franklin [3], Janach [4], Mogi [5–7], Yumlu and Ozbay [8], Hoek and Bieniawski [9], Brace et al. [10], Wang and Shrive [11] amongst others. The final failure planes observed in unconfined compressive strength (UCS) tests or extension tests are generally parallel to the direction of maximum compressive stress, whereas in standard triaxial tests with confinement they are generally at some specific angle. Similar observations are made in the mining environment, where the absence of confinement in material adjacent to

excavations or in mining pillars causes fracturing parallel to the maximum compression direction resulting in so-called slabbing, as shown in Fig. 1(a) and (b). The ultimate aim of the model is to predict the development of fracturing around an advancing stop face in a deep level mine. As shown in Fig. 1(c), the rock mass is extremely fractured, with fractures forming in uniaxial compression at the face and in extension as the rock moves into the excavated region. In addition, in confined regions ahead of the mining face the rock fails in a mechanism similar to that of a conventional triaxial test with oblique failure planes resulting in shear deformation evolve making specific angles with the maximum compressive stress direction. The model, therefore, must be able to predict the simultaneous formation of fractures due to all these different mechanisms. It is noted that the extension test, conventional triaxial test and the uniaxial compression (UCS) test only provide insight into the material response to stress states on the boundary of the full stress domain. Unfortunately, these experiments do not truly isolate the material response, but reflect the response of the complete experimental system. It is therefore necessary that due consideration be given to such factors as specimen boundary conditions (end effects), stiffness of the testing apparatus and loading rate [5,12].
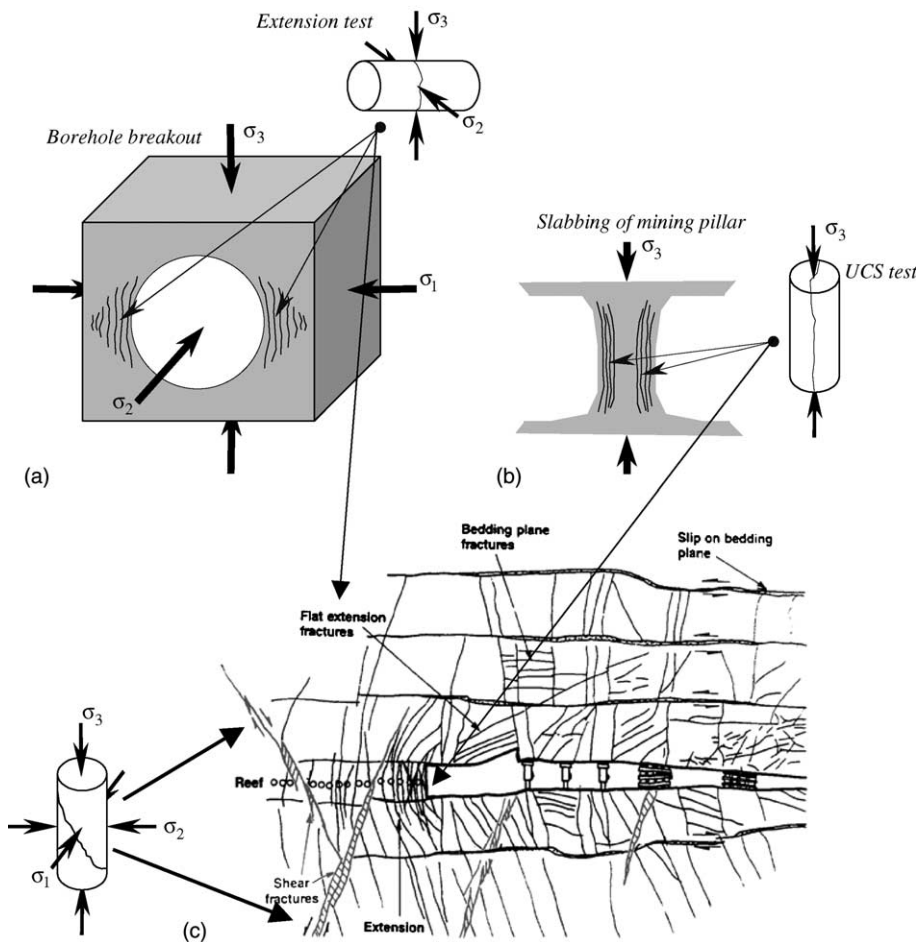

Fig. 1. Equivalence of experiment and in situ mining stress states. (a) The extension test and the unconfined walls of excavations, (b) the uniaxial compression test (UCS) and unconfined rock pillars and (c) the triaxial test and the highly confined compression zone ahead of the deep level mining face, after Ortlepp [21].

The theory of the nucleation and growth of microcracks from pre-existing flaws is attributed to Griffith [13] and is fundamental to the understanding of the quasi-brittle fracture process. Cracks initiating from flaws grow and become stable, a process that is repeated for less critical flaws as the stress is raised, resulting in stable pre-peak inelasticity [10,14–18]. Dilatancy is the most significant manifestation of quasi-brittle fracture in compression and is defined as the increase in volumetric strain relative to the expected elastic response [2]. Using acoustic emission Scholz [19] confirmed the observation of Brace et al. [10] that dilatancy is directly proportional to microfracturing. Crack growth orthogonal to the direction of dilation (parallel to the maximum compression stress) does not immediately produce a mechanical instability, as observed in tensile fields. The direction of fracture propagation is necessarily orthogonal to the maximum extensional strain and generally coincides with the direction of maximum applied compressive stress [15]. It is this stable fracture process in compression that results in the large differences between tensile and compressive strengths of quasi-brittle materials. This process ultimately leads to mechanical instability in the post-peak region resulting in the formation of a macroscopic failure plane from the coalescence and complex interaction of microcracks and the heterogeneous microstructure [1,2,15,20]. The post-peak drop in strength that occurs is associated with the rupture of material linkages and the mobilisation of the macroscopic failure plane.

This creates a global deformation mechanism that is generally associated with significant energy release and may be the cause of so-called rockbursts, occurring when failure planes extend into mining excavations [21].

Many complex numerical models invoking the concepts of elastoplasticity, damage mechanics and statistical methods have been presented in the computational literature [22,24–26], but many are not widely used due to the difficulty in determining material parameters and the high level of technical expertise required by the user. The aim of this paper is to present a pragmatic and relatively simple numerical model for the degradation and subsequent discrete fracturing of quasi-brittle materials in compression. To this end the widely used Mohr–Coulomb failure criterion is adapted and coupled with a fully anisotropic tensile smeared crack model. The Mohr–Coulomb criterion is able to recover the salient features of the quasi-brittle response within engineering accuracy, including dilation and has the advantage of being based on parameters that are easily determined experimentally. Fracturing due to dilation is accommodated by introducing an explicit coupling between the inelastic strain accrued by the Mohr–Coulomb yield surface and the anisotropic degradation of the mutually orthogonal tensile yield surfaces. The introduction of discrete fractures into the material is achieved by modification of the finite–discrete element code ELFEN [23,27], which allows the finite element continuum to fracture into discrete blocks based on the selected failure criterion. The existing fracture and contact logic was designed for tensile fracture with little post-fracture interaction of the fractured rock, and had to be modified for the compressive stress regime where fractured subregions interact and slide relative to each other after the initiation of fracturing. The proposed model represents a phenomenological approach in which micromechanical processes are only considered in terms of the average global response. Isotropy of strength in compression is justified by assuming uniform material heterogeneity, while accrual of inelastic strain and associated degradation of the tensile strength is necessarily anisotropic and dependent on the loading direction. The effectiveness of the proposed numerical model will be assessed by application to problems such as triaxial and plane strain rock tests, borehole breakouts and strip punch tests.

2. Modelling of discrete fracture

2.1. The discrete/finite element method

The spatially discretised form of the dynamic equilibrium equations at time ^Nt is given by [23,24,28],

$$\mathbf{M}\ddot{\mathbf{u}}(^Nt) + \mathbf{C}\dot{\mathbf{u}}(^Nt) = \boldsymbol{f}^{\mathrm{ext}}(^Nt) - \boldsymbol{f}^{\mathrm{int}}(\mathbf{u}(^Nt)). \tag{1}$$

The diagonal mass matrix, $\mathbf{M}$ is defined by,

$$\mathbf{M} = \underset{e=1}{\overset{\text{nelem}}{\mathbf{A}}} \sum_{i=1}^{\text{nnode}} \int_{e_V} {}^e\boldsymbol{\rho}\mathbf{N}_i^{\mathrm{T}}[\mathbf{N}_1, \mathbf{N}_2, \ldots, \mathbf{N}_{\text{nnode}}] \, \mathrm{d}V \tag{2}$$

and $\mathbf{C}$ is the diagonal damping matrix ($\mathbf{C} = \alpha\mathbf{M}$) defining the viscous damping term with constant factor α. It is apparent that at discrete time ${}^Nt$ equations (1) represent a coupled system of second order linear differential equations with constant coefficients. The relevant class of initial boundary value problems is recovered by invoking (2) and the necessary boundary conditions and initial values. Using a central difference time integration scheme and adopting a diagonal damping matrix $\mathbf{C}$ recovers the algebraic equation for the velocity of the degree of freedom u_i at time ${}^{N+1}t$, giving,

$$^{N+\frac{1}{2}}\dot{u}_i = \frac{2M_{ii} - C_{ii}{}^N\Delta t}{2M_{ii} + C_{ii}{}^{N+1}\Delta t} {}^{N-\frac{1}{2}}\dot{u}_i + 2^{N+\frac{1}{2}}\Delta t \frac{f_i^{\text{ext}}({}^Nt) - f_i^{\text{int}}(\mathbf{u}({}^Nt))}{2M_{ii} + C_{ii}{}^{N+1}\Delta t}. \tag{3}$$

The displacement at time ${}^{N+1}t$ is given by,

$$^{N+1}u_i = {}^Nu_i + {}^{N+\frac{1}{2}}\dot{u}_i{}^{N+1}\Delta t. \tag{4}$$

The amount of damping selected depends on whether the problem is dynamic or quasi-static. For quasi-static analyses, a dynamic relaxation approach is taken with a higher damping value of 0.3 leading to convergence to the static solution after sufficient timesteps. It is noted that the use of difference equations requires special consideration for initial conditions and prescribed quantities. The objective Green–Naghdi stress update procedure [29], rotates the spatial state variables to the reference configuration in which classical (material-non-linear-only) elastoplasticity is invoked to update the stress rate. It has been observed that the Green–Naghdi stress rate is suitable for materials under small elastic strain conditions [24,30,31]. The kinematics of a general quasi-brittle discrete system is that of large displacements, large rotations and small strain. The clear separation between kinematic non-linearity and material non-linearity, permits the use of a small strain inelastic stress update in the reference configuration. The updates for the compression, tension and extension stress regimes are described in the following sections.

2.2. Mohr–Coulomb model for compression

The Mohr–Coulomb criterion is used for the failure envelope in compression as a first order approximation equating the shear failure stress τ to the sum of the internal friction and the inherent material cohesion c_0, giving,

$$|\tau| = c_0 - \sigma_{\mathrm{n}} \tan \phi = c_0 - \sigma_{\mathrm{n}}\mu, \tag{5}$$

where ϕ is the internal friction angle and μ is the coefficient of friction. It is noted that the normal stress σ_{n} acting on an inclined plane is defined here to be negative in compression.

The Mohr–Coulomb failure criterion in principal stress space is given by,

$$\tfrac{1}{2}(\sigma_{\max} - \sigma_{\min}) + \tfrac{1}{2}(\sigma_{\max} + \sigma_{\min}) \sin \phi = c_0 \cos \phi, \tag{6}$$

where $\sigma_{\max}$ and $\sigma_{\min}$ are the maximum (most tensile) and minimum (most compressive) principal stresses respectively, and are shown in Fig. 2. The linear approximation of the Mohr–Coulomb model is poorest at low confinement, where the experimental strength-confinement curves exhibit greatest non-linearity (convexity), but for many materials is a reasonable approximation for confinements below the brittle–ductile transition. The Mohr–Coulomb failure criterion is independent of the intermediate principal stress σ_2 resulting in the failure plane manifesting itself necessarily parallel to this direction. The poor approximation of the tensile region of the conventional Mohr–Coulomb yield surface to the mutually orthogonal tensile
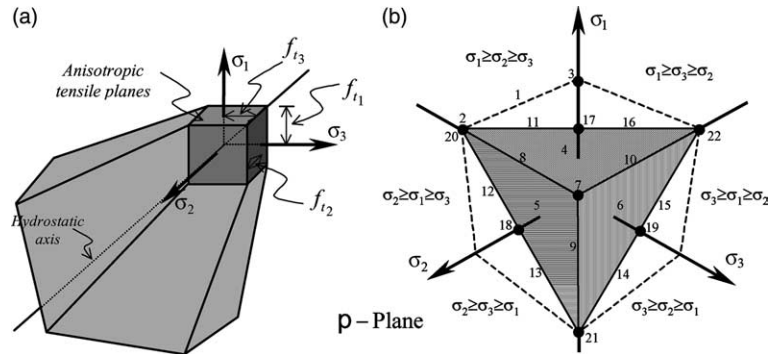
Fig. 2. The compressive fracture model. (a) The isotropic Mohr–Coulomb yield surface with softening anisotropic tensile planes and (b) Pi-plane representation indicating possible return-mappings.

planes is a major shortcoming in terms of application to quasi-brittle fracture and is addressed later in this paper.

It is necessary to introduce so-called mobilised material parameters that realise hardening/softening with respect to some hardening parameter such that the permissible elastic domain depends on the current state of inelastic strain as well as the history of evolution. The effective plastic strain $\bar{\varepsilon}^{\mathrm{p}}$ is adopted here and at time t is defined by,

$$\bar{\varepsilon}^{\mathrm{p}}(t) = \int_0^t \sqrt{\frac{2}{3}\dot{\boldsymbol{\varepsilon}}^{\mathrm{p}} : \dot{\boldsymbol{\varepsilon}}^{\mathrm{p}}}\, \mathrm{d}t, \tag{7}$$

where $\dot{\boldsymbol{\varepsilon}}^{\mathrm{p}}$ is the inelastic strain rate tensor. The form of the hardening/softening curves for the mobilised cohesion $c_0(\bar{\varepsilon}^{\mathrm{p}})$ and the mobilised friction angle $\phi(\bar{\varepsilon}^{\mathrm{p}})$ are established by considering laboratory test data. A non-associative implementation of the Mohr–Coulomb elastoplasticity model is required for the recovery of the correct physical dilation response in compression. Replacing the friction angle ϕ in the Mohr–Coulomb yield function (6) by the so-called dilation angle ψ, such that $\psi < \phi$, recovers the widely adopted plastic flow potential Ψ given by,

$$\Psi(\sigma, \bar{\varepsilon}^{\mathrm{p}}) = \tfrac{1}{2}(\sigma_{\max} - \sigma_{\min}) + \tfrac{1}{2}(\sigma_{\max} + \sigma_{\min})\sin\psi - c_0\cos\psi, \tag{8}$$

where $c_0 = c_0(\bar{\varepsilon}^{\mathrm{p}})$, $\psi = \psi(\bar{\varepsilon}^{\mathrm{p}})$. The relationship between the dilation angle ψ and observed dilatancy is defined by the constant dilatancy observed near the peak stress. After the formation and subsequent mobilisation of a macroscopic failure plane the dilation tends to zero.

Stress states falling outside the elastic domain are non-permissible and are returned to the yield surface through the so-called return-mapping procedure that is associated with the accrual of inelastic strain. It is the dependency of the yield surface on the inelastic strain that renders the return-mapping non-linear and necessitates the adoption of an iterative Newton–Raphson solution scheme. The flow rule defines the evolution of inelastic strain through the concept of the subgradient of a function and is referred to as Koiter's rule for the case of multisurface plasticity [32], giving,

$$\dot{\boldsymbol{\varepsilon}}^{\mathrm{p}} = \sum_{\alpha=1}^{m} \dot{\lambda}_\alpha \partial_\sigma \Psi_\alpha(\boldsymbol{\sigma}, \kappa), \tag{9}$$

where $\Psi_\alpha(\boldsymbol{\sigma}, \kappa)$ is the plastic flow potential function and λ_α is the corresponding plastic consistency parameter (or plastic multiplier) for the yield function $f_\alpha(\boldsymbol{\sigma}, \kappa)$, with $\alpha \in [1, 2, \ldots, m]$. For non-associative plasticity $\Psi_\alpha(\boldsymbol{\sigma}, \kappa) \neq f_\alpha(\boldsymbol{\sigma}, \kappa)$ for some $\alpha \in [1, 2, \ldots, m]$. The Kuhn–Tucker complementary (loading/

unloading) conditions are the optimality conditions for the closest point projection minimisation problem and for all $\alpha \in [1, 2, \ldots, m]$ are given by,

$$\dot{\lambda}_\alpha \geqslant 0, \quad f_\alpha(\boldsymbol{\sigma}, \kappa) \leqslant 0, \quad \dot{\lambda}_\alpha f_\alpha(\boldsymbol{\sigma}, \kappa) = 0. \tag{10}$$

The consistency (persistency) condition is given by,

$$\dot{\lambda}_\alpha \dot{f}_\alpha(\boldsymbol{\sigma}, \kappa) = 0. \tag{11}$$

If $m_{\mathrm{adm}} \leqslant m$ is the number of constraints at a certain point $(\boldsymbol{\sigma}, \mathrm{k}) \in \partial E_\sigma$, with associated indices belonging to the set $J_{\mathrm{adm}} = \{\beta \in [1, 2, \ldots, m] | f_\beta(\boldsymbol{\sigma}, \kappa) = 0\}$, then the actual active constraint set J_{act} is defined by,

$$J_{\mathrm{act}} = \{\alpha \in J_{\mathrm{adm}} | \dot{f}_\alpha(\boldsymbol{\sigma}, \mathrm{k}) = 0\}. \tag{12}$$

It is the determination of the actual active constraint set J_{act} that is one of the principal algorithmic concerns in multisurface plasticity.

2.3. The tensile fracture model

The multiple fixed crack model [33] and the microplane model [34] are attempts to overcome the limitations of the fixed crack [34] and rotating crack [37] concepts. The differences between these models are discussed in detail elsewhere [24,36]. In fixed crack models, the elastic properties degrade or plastic strain accumulates across a pre-defined plane inducing a coupling between the shear and normal stresses. The rotating crack concept has no memory of the crack direction and damage accrues in the direction of the current principal stresses [36].

The fixed crack model is observed to be overly constrained with induced shear stresses unable to invoke effective reorientation of crack directions, as is the physical manifestation. Conversely, the rotating crack model is under constrained, exhibiting much-reduced shear stresses (for coincident rotation of principal stress and strain). The crack direction reflects the current state of damage and not the damage history. In oscillating stress fields that realise large rotations of the principal directions, it is possible that the introduced discrete fractures will not reflect the previous history of directions in which damage was accrued. The multiple fixed crack model and the microplane model allow simultaneous cracking in multiple orientations which relieves excessive shear constraints while introducing strong path dependence. However, these models are overly complex for the simplifying assumptions on which they are based and generally exhibit arbitrary coupling between damage directions and spurious energy dissipation.

The stabilised rotating crack model is now proposed that realises crack band orientations defined by the weighted average of the extensional strain directions invoking damage. The crack band remains fixed during unloading and reloading, with the average orientation reflecting the cracking history and thus constraining spurious rotation. Reorientation of the crack band in response to a build up of shear stress relaxes the fixed crack constraints during loading and more closely resembles the physical manifestation.

To determine the crack direction, consider a two-dimensional configuration at time $^N t$ consisting of a single crack band with normal $\mathbf{n}$ at an average angle $^{N_t}\boldsymbol{\theta}_{\mathrm{av}}$ to an appropriate reference frame (global or local element) given by,

$$^{N_t}\boldsymbol{\theta}_{\mathrm{av}} = \frac{\sum_{t=0}^{N_t} \Delta^t \boldsymbol{\omega}_{nn} {}^t\boldsymbol{\theta}_{\varepsilon_1}}{\sum_{t=0}^{N_t} \Delta^t \boldsymbol{\omega}_{nn}}, \tag{13}$$

where $\Delta^t \boldsymbol{\omega}_{nn}$ is the increment of scalar damage in direction $\mathbf{n}$ at time t and $^t\boldsymbol{\theta}_{\varepsilon_1}$ is the angle of the first principal strain direction with respect to the reference frame at time t. Generally, the orientation of maximum applied strain $\boldsymbol{\theta}_{\varepsilon_1}$ does not coincide with the crack band normal orientation $\boldsymbol{\theta}_{\mathrm{av}}$, but with damage

accrual in a given direction they are convergent. In 3-D the average orthotropic orientation is more complicated, but can be derived in terms of direction cosines.

It is apparent that the stabilised rotating crack model violates the form invariance condition due to the general non-coincident rotation of the principal axes of stress and strain. However, for systems which experience large arbitrary rotations of crack bands due to dynamic effects, unloading or post-failure interaction, the error introduced due to the omission of shear coupling terms is negligible compared to that introduced through spurious crack band orientations. It is noted that fracture is an extensional process and the modelling of the normal behaviour is of primary importance.

The manifestation of deformation during fracturing is accomplished with a crack band model [34,35,38]. This model exhibits a constant strain distribution and a linear variation of displacement across the width of the band, whereas a cohesive crack model [39–41] exhibits a Dirac delta (spike) strain function and a corresponding displacement jump across the crack. The crack band description is therefore more realistic at the initiation of softening, where material damage is dispersed, while a cohesive crack is more realistic at the end of softening, where dispersed damage coalesces to form a localised discrete crack. The deformation in a crack band is equivalent to that of a cohesive crack if the fracturing elongation $\Delta L^f = \varepsilon^f h_c$ is identified with the cohesive crack opening displacement w, such that $w = \varepsilon^f h_c$. Identical stress-elongation curves for the crack band model and the cohesive crack model require a correspondence between the constitutive functions. It would appear that although the cohesive crack model and the crack band model are equivalent, the crack band model has an extra parameter in the crack band width h_c. Recognising that the crack band width h_c is used in defining the specific fracture energy, the crack band model is equivalently defined in terms of a tensile strength f_t and a specific fracture energy G_f that defines the amount of energy dissipated per unit cross-sectional area of the crack band.

The crack band model can be formulated with many different strain-softening curves to describe the energy dissipation. In general, exponential curves appear to yield better results when applied to concrete systems [4,13,18,41], although this is not necessarily true for brittle fine-grained rocks and ceramics. Nonetheless, the linear softening curve is able to recover the salient features of the quasi-brittle structural response and is applied here as a useful first order approximation. For an arbitrary finite element mesh strain-softening will necessarily localise into a single element of local length scale (average dimension) $h_c^{(e)}$ and mesh objective dissipation of the specific fracture energy G_f is achieved here using a linear strain-softening curve defined by,

$$\boldsymbol{\sigma} = \phi(\boldsymbol{\varepsilon}^f) = f_t\left(1 - \boldsymbol{\varepsilon}^f/\boldsymbol{\varepsilon}_c^{f(e)}\right), \tag{14}$$

where $\boldsymbol{\varepsilon}_c^{f(e)}$ is the element critical fracturing strain given by,

$$\boldsymbol{\varepsilon}_c^{f(e)} = \frac{2G_f}{h_c^{(e)} f_t}. \tag{15}$$

For the crack band model with linear strain softening, the constant softening modulus H of the element has a bi-linear behaviour given by,

$$H = \frac{\mathrm{d}\sigma}{\mathrm{d}\varepsilon^p} = -\frac{h_c^{(e)} f_t^2}{2G_f} \quad \text{for } \varepsilon^{f(e)} \leqslant \varepsilon_c^{f(e)},$$
$$H = 0 \quad \text{for } \varepsilon^{f(e)} > \varepsilon_c^{f(e)}, \tag{16}$$

where $h_c^{(e)}$ is the local element lengthscale (average dimension) and G_f is the specific fracture energy.

The selected implementation of the anisotropic rotating crack band model consists of three orthogonal tensile planes

$$f_i^{\sigma_i}(\boldsymbol{\sigma}) = \sigma_i - f_{ti} - H\langle\Delta\varepsilon_i^p\rangle = 0 \tag{17}$$

that act independently in each of the principal stress σ_i directions and can thus realise anisotropic softening in the material. Fig. 2(a) shows the coupling of the orthogonal, anisotropic tensile planes and the isotropic Mohr–Coulomb yield surface, while Fig. 2(b) shows the Pi-plane representation of the composite yield surface. The incremental update of the tensile strength in each of principal stress direction is given by,

$$^{n+1}f_{t_i} = {}^{n}f_{t_i} + H\langle\Delta\varepsilon_i^p\rangle \quad \text{for } i = 1, 2, 3,\tag{18}$$

where $\langle\cdot\rangle$ are the McAuley brackets returning zero for negative (compressive) inelastic strain increments $\Delta\varepsilon_i^p$, and $^0f_{t_i} = f_t$. Tensile strengths associated with the principal stress directions at the end of the previous timestep are associated with the current principal stress directions according to the relative proximity of orientation. The assumptions on which the rotating crack band model is based restrict approximate validity to only small rotations of the stress field. Any violation of tensile constraints, whether by the elastic trial state or induced during the standard Mohr–Coulomb return-mapping, necessarily introduces the possibility of a consistent return-mapping to any feasible combination of the tensile planes and the Mohr–Coulomb yield surface. This is a consequence of the anisotropy of the tensile response, that no longer ensures the validity of the constraint $\sigma_1 \geqslant \sigma_2 \geqslant \sigma_3$ for the updated principal stresses.

2.4. Explicit coupling between degradation in compression and tension

Starting from the assumption that quasi-brittle fracture is extensional in nature, any phenomenological yield surface is effectively divided into regions in which extensional failure can be modelled directly, as in the case of tensile stress fields and indirectly, as in the case of compressive stress fields. The violation of either region of the yield surface should result in the realisation of inelastic extensional strain (cracks opening). In both cases the definition of this inelastic strain is identical, it is the micro-mechanism that produces the strain that differs. Fig. 3 depicts the dilation response of compressive failure in quasi-brittle materials and clearly indicates the extensional inelastic strain directions associated with fracture. The vector of principal increments of inelastic strain obtained from the single vector return-mapping to the Mohr–Coulomb main-plane is given by [24],

$$\Delta\bar{\varepsilon}^p = \begin{Bmatrix} \Delta\varepsilon_1^p \\ \Delta\varepsilon_2^p \\ \Delta\varepsilon_3^p \end{Bmatrix} = \Delta\lambda_\alpha \begin{Bmatrix} 1 + \sin\psi \\ 0 \\ \sin\psi - 1 \end{Bmatrix},\tag{19}$$

where the increment of inelastic strain $\Delta\varepsilon_1^p$ in the first principal stress direction is extensional. An explicit coupling is therefore proposed between the extensional inelastic strain associated with the dilation response of compressive failure and the tensile strength in the dilation direction, even in the absence of tensile stress.
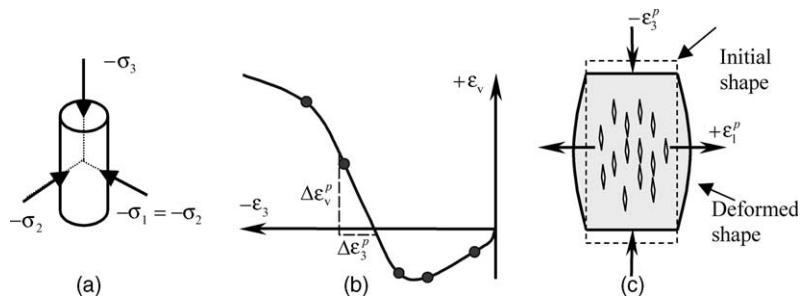

Fig. 3. (a) Compressive loading with confining stress, (b) relationship between applied and volumetric strain and (c) compressive failure with associated lateral extensional (positive) inelastic strain causing fracture and dilation.

Various methods have been applied for modelling of biaxial stress states e.g. [25,26,36]. The proposed implementation of an explicit coupling between compressive stress induced extensional strain and tensile strength degradation permits the realisation of discrete fracturing in purely compressive stress fields. Such increments of extensional strain must be associated with tensile strength degradation in the parallel direction, giving,

$$f_{ti} = f_{ti}(\varepsilon_i^p) \quad \text{where } \varepsilon_{i_{n+1}}^p = \varepsilon_{i_n}^p + \Delta\varepsilon_i^p, \tag{20}$$

where f_{ti} is the tensile strength in the *i*th principal stress direction. Thus, for the example shown in Fig. 3c, $i = 1$. In pure, triaxial, tension, the strength degradation will occur in all three principal stress directions. For a biaxial state of stress with one direction in tension, and the orthogonal direction in compression, the degradation will occur perpendicular to the tensile stress, with the possibility of additional damage occurring in the same direction if the compressive stress exceeds the strength.

The update of the tensile strength is only performed once consistency has been achieved for a return-mapping including a compressive yield surface. It is noted that the tensile strength in a particular direction is not updated if the associated tensile yield plane is included in the consistent return-mapping. The principal stress return-mapping is a specialisation of the standard elastic predictor/plastic corrector schemes widely employed in computational plasticity [29], with the return-mapping procedure (associated with the plastic corrector phase) carried out in the principal stress space. This differs markedly from the Mohr–Coulomb implementations generally encountered in the literature that adopt the invariant representation of the model. The principal stress approach adopted here results in a far simpler and more efficient computational implementation. It appears that most non-linearities of the return-mapping are confined to the spectral decomposition, whereby the principal stresses are evaluated as non-linear functions of the stress tensor. The feasible return-mappings are numbered in Fig. 2(b) and detailed by Klerck [24]. The two algorithms proposed by Simo et al. [42] for calculating the return to the active yield surface assume that the final successful return-mapping includes the initial set of trial constraints. This is not always the case for the current model and so an algorithm proposed by Perić and de Souza Neto [44] is adopted that assumes nothing about the nature of the successful return-mapping and exhibits the ability to attempt all permissible constraint combinations. Generally it is impossible to predetermine which return-mapping will be successful and it is therefore necessary to design an algorithm that is able to attempt all return-mappings in turn until consistency is achieved. In an attempt to maximise computational efficiency it is possible to order the return-mappings with respect to feasibility and eliminate return-mappings that are known not to be feasible. A discrete crack is introduced when the tensile strength in a principal stress direction reaches zero and is orientated orthogonal to this direction.

2.5. The topological update

A discrete crack is introduced when the tensile strength in a principal stress direction reaches zero and is orientated orthogonal to this direction, as already described with respect to the crack band model. The insertion of discrete cracks into the quasi-brittle continuum follows three steps.

Step 1. Create a non-local failure map (weighted nodal averages).
Step 2. Determine fracture feasibility and the order of discrete crack insertion.
Step 3. Perform the topological update (remeshing).

The most meaningful quasi-brittle damage indicator or so-called failure factor is the ratio of the inelastic fracturing strain ε^f to the critical fracturing strain ε_c^f. The local fail factor F_k at Gauss point *k* is given by,

$$F_k = (\varepsilon^f / \varepsilon_c^f)_k, \tag{21}$$

where F_k is associated with a local fracture direction θ_k, which is normal to the local failure (softening) direction. Discrete fracture at the Gauss point level is effectively realised on dissipation of the complete fracture energy (zero strength) and corresponds to a failure factor greater than unity. However, the nodal basis of the finite element discretisation renders discrete crack insertion simpler if associated with nodal failure factors. It is with this motivation that a non-local failure map is sought, based on the weighted nodal averages of immediately adjacent element (Gauss point) failure factors and fracture directions. The weighted-average failure factor $\overline{F}_p$ and fracture direction $\overline{\theta}_p$ at node p are given by,

$$\overline{F}_p = \sum_{k=1}^{N_{\mathrm{adj}}} F_k w_k \Bigg/ \sum_{k=1}^{N_{\mathrm{adj}}} w_k, \quad \overline{\theta}_k = \sum_{k=1}^{N_{\mathrm{adj}}} \overline{\theta}_k w_k \Bigg/ \sum_{k=1}^{N_{\mathrm{adj}}} w_k, \tag{22}$$

where N_{adj} is the number of immediately adjacent Gauss points and w_k is a weighting factor usually taken as the element volume.

A discrete fracture will necessarily be realised through a nodal point if the nodal failure factor is greater than unity. The possibility of adjacent nodes reaching failure factors greater than unity within the same time increment renders it necessary to determine a discrete fracture sequence prior to updating the topology. It is apparent that the sequence can affect the final fracture pattern. The physical manifestation of multiple crack propagation is firmly based on energetic feasibility, with the most energetically feasible fracture propagating first. The magnitudes of the failure factors represent the numerical analogy of energetic feasibility and their relative magnitudes determine the sequence of topological update.

The discrete crack insertion and the associated topological update commences with the definition of a fracturing plane through the failed nodal point and in the direction of the weighted average fracture direction, as shown in Fig. 4(a). The plane represents the actual discrete crack orientation and does not generally coincide with the existing element sides. Insertion of the actual crack direction therefore requires local remeshing and the possible creation of new elements, as shown in Fig. 4(b). This intra-element fracturing may result in the creation of unfavourably dimensioned sliver elements if the underlying discretisation is simply split and may decrease the time increment stability limit. In this case local adaptive mesh refinement must be undertaken to achieve an acceptable element topology. Alternatively, an element threshold dimension can be defined below which the discrete crack is snapped to the most favourably orientated existing element side, as shown in Fig. 4(c). Inter-element fracturing in which no remeshing is considered is not usually desirable, requiring very fine meshes to capture the fracture directions accurately.

Following discrete crack insertion the failed elements are reinitialised under the assumption that the element damage is coalesced into the discrete crack formation. Ideally only the damage normal to the discrete crack should be zeroed, but with remeshing and the creation of additional elements the complexity of state variable mapping is avoided by assuming that all state variables in the failed elements are reinitialised.

The contact response of the newly created surfaces is of vital importance to the stability of the solutions after fracture initiation. The conventional approach for discrete contact in finite element methods is to
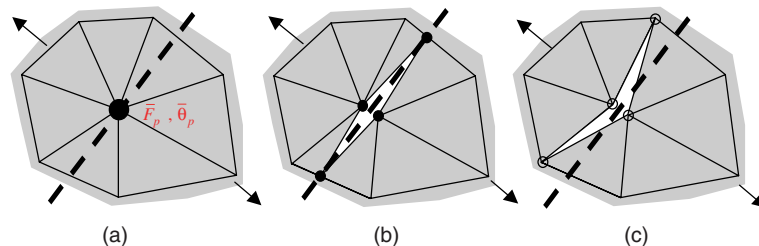

Fig. 4. (a) Weighted-average nodal failure direction, (b) intra-element fracturing and (c) inter-element fracturing (the dashed lines denote the potential crack planes and the arrows indicate the fracturing strain direction).

apply the penalty method to approximately satisfy the contact displacement constraints for finite penalty coefficients [27,43]. This results in the finite penetration of contact surfaces and an effective reduction in the volume of contacting entities. This causes an instability when the region is in compression resulting in spurious energy release. Thus, the correct contact description requires the exact satisfaction of the displacement constraint. The explicit Lagrangian method was proposed for the determination of the contact forces that satisfy the displacement constraints exactly [45,46]. The classical Lagrange multiplier method evaluates the contact forces exactly, but is not compatible with the explicit integration operator. Explicit compatibility is established by referencing Lagrange multipliers (contact forces) one time increment ahead of associated surface contact displacement constraints. The explicit Lagrange multiplier method is not purely explicit because a coupled system of equations must be solved to obtain the Lagrange multipliers. The equation solving strategy adopted here is the symmetric Jacobi method, in which non-linear contact force conditions (normal tension limit and tangential friction) are enforced during each iteration [24]. Tangential displacement constraints (friction) are enforced using the penalty method. For a stable solution, the explicit Lagrange multiplier method requires a reduction in the critical time step to one-tenth of the critical timestep for the continuum analysis. The classical non-associative Coulomb friction law defining a critical tangential force proportional to the normal contact stress, $f_\mathbf{n}$ and frictional coefficient μ is applied once the fracture has been placed in the finite element mesh.

Discrete fracture is realised after localisation of damage into crack bands and is therefore prone to the discretisation dependence of the smeared crack models. This affects the positioning and the spacing of fractures, but not the predicted orientation. The orientation is determined by the non-local averaging of local element failure directions and is effectively independent of the discretisation. As already mentioned, discretisation dependence can be minimised by utilising high-density, non-biased meshes of low order elements. The context in which discrete fracturing has been introduced so far has been that of localised failure in individual crack bands. This type of failure generally originates from structural features that concentrate stress. Generally, objective fracture energy dissipation for distributed failure requires the use of regularisation methods that ensure objective dissipation over finite volumes through the introduction of a spatial lengthscale, which have been considered elsewhere [24].

3. Numerical examples

3.1. The strip punch test

Consider the strip punch test investigated experimentally by Dede [47] for quartzite rock to simulate the failure of stabilising pillars in deep level gold mines. Prismatic quartzite specimens of dimensions $80 \times 80 \times 80$ mm were machined on one side to produce a bisecting 1 mm high and 10 mm wide strip, as shown in Fig. 5(a). The normal loading of the raised strip was performed within a triaxial loading cell, with 4.5 MPa of confining pressure applied to the specimen sides. To reduce friction all loading surfaces were coated with stearic acid and so the platen friction coefficient is set to 0.005. The material friction coefficient is selected to be 1.2.

Although the stress state is three-dimensional, the geometry can be well described in plane strain. The adopted plane strain finite element mesh is shown in Fig. 5(b) and consists of a graded distribution of three-noded, linear elements with single point Gaussian quadrature. The mesh is observed to be refined in the region of the punch strip, with elements of dimension 1 mm. The 4.5 MPa confining pressure is applied to the specimen via discrete steel platens (shown in dark) and the normal strip load or axial load is applied via a prescribed velocity of 0.1 m s^{-1}. Material properties for quartzite are defined by Dede [47]. The input material parameters and the evolution of the cohesion, friction and dilation were found by matching the results of a single element triaxial test simulation with the data [47] and are given in Table 1. The Young's modulus is 68 GPa, the Poisson's ratio is 0.17, the density is 2800 kg m^{-3}, the tensile strength is 27 MPa.

Fig. 5. (a) Strip punch geometry and loading configuration, after Dede [47] and (b) plane strain finite element model.

As mentioned in Section 2.5, the introduction of discrete fracturing requires a reduction in the critical time step to a tenth of the continuum value. The timestep for the discrete fracture model is 0.49E−8 s and the model takes 8.5 h to run on a 1.8 GHz computer, compared to 57 min for the continuum models. Thus, the effect of varying the fracture energy was studied using continuum analyses to save time and to provide a comparison to evaluate the effect of introducing the discrete fractures. Fig. 6(a) shows a typical plot of the experimental normal punch stress versus the specimen axial strain and the plots recovered from the numerical system. The initiation of purely compression induced microfracturing occurs at the edges of the punch strip, where high compressive stress concentrations exists. The first significant feature of the axial stress–strain response defined in Fig. 6(a) is the drop in stress experienced between points A and B. This stress drop is associated with the localisation and coalescence of material degradation about the periphery of the conical microfracture zone to form the macroscopic failure zone shown in Fig. 7(a). The hardening of the axial stress–strain response between points B and C is attributed to the continued formation and mobilisation of the conical failure zone and the initiation of the downward wedging action. The purely tensile nature of the stress field propagating the cleavage crack is verified by observing the absence of significant compressive inelastic strain vectors beneath the conical microfracturing zone, as shown in Fig.

Table 1
Evolution of material parameters with plastic strain for three rock types

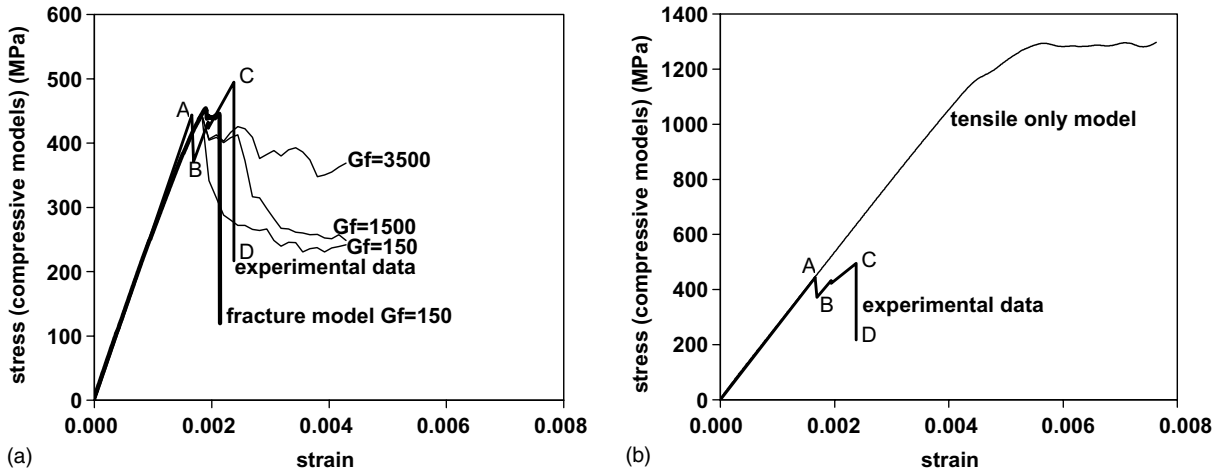| *Quartzite*								
Plastic strain	0	0.0005	0.001	0.0015	0.002	0.004	0.008	0.03
Cohesion (MPa)	53	50	45	42	37	28	10	10
Friction angle (°)	5	28	34.8	38.8	43.2	46	46	46
Dilation angle (°)	0	28.4	28.4	28.4	28.4	28.8	20	20
Sandstone								
Plastic strain	0	0.0005	0.001	0.0015	0.002	0.008	0.01	0.03
Cohesion (MPa)	20	19	18	17	16	4	0	0
Friction angle (°)	17	31.5	40.5	52.5	52.5	52.5	52.5	52.5
Dilation angle (°)	0	5.75	11.5	17.25	23	23	18	4
Tyndall limestone								
Plastic strain	0	0.0005	0.002	0.0055	0.011	0.02	0.022	0.03
Cohesion (MPa)	14	14	13	11	8	4	4	4
Friction angle (°)	4.4	22.4	27.2	29.2	29.6	30.4	30.4	30.4
Dilation angle (°)	0	19.6	19.6	19.6	19.6	19.6	5	5

Fig. 6. (a) Numerical axial stress vs. axial strain plot for compressive fracture models with different parameters. Experimental data after Dede [47]. (b) Numerical axial stress vs. axial strain plot for tension only fracture model.
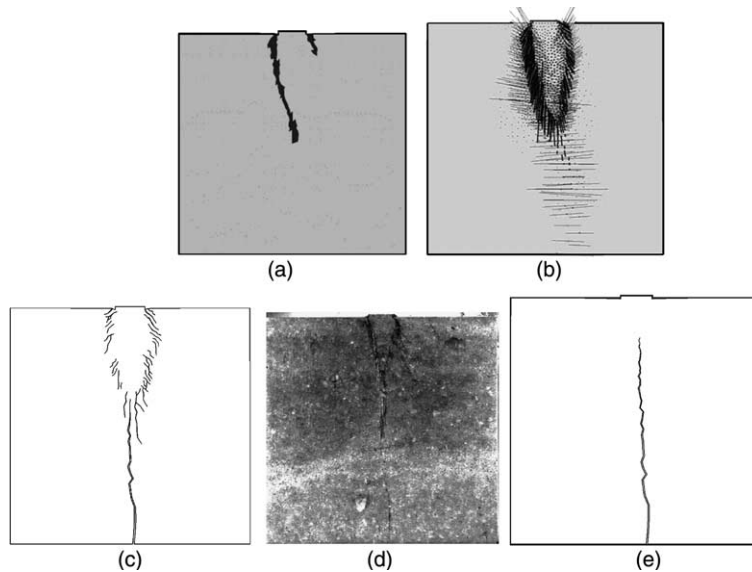

Fig. 7. (a) Initiation of material degradation at the edges of the punch strip, (b) plastic strain vectors describing the conical micro-fracture zone beneath the punch strip, (c) full mobilisation of the conical microfracture zone beneath the punch strip and completed formation of the axial cleavage crack, (d) the observed fracture pattern and (e) discrete fracture pattern for a tension only model.

7(b). The formation of the axial cleavage crack and the full mobilisation of the conical zone beneath the punch strip produces a global deformation mechanism resulting in the complete failure of the specimen between points C and D with a fracture pattern as shown in Fig. 7(c). The numerical discrete fracture pattern compares very well with the typical experimental fracture pattern presented by Dede [47] and shown in Fig. 7(d). The en-echelon fractures about the periphery of the conical zone are clearly observed, as is the

axial cleavage crack. Some coalescence of the en-echelon fractures is observed in the numerical fracture pattern, although it is noted that the spacing of cracks is necessarily set by the mesh and the recovery of a complete failure surface on which sliding can be realised would require considerable mesh refinement. The conical zone beneath the punch strip in the numerical model is observed to be longer than that observed in experimental results. This difference is attributed to the effect of mesh alignment on the local numerical model. The data presented by Dede [47] shows the overall deformation of the test machine and the loading platens. The deformations were multiplied by a calibration factor of 0.24 to produce the response across the sample only.

The graph in Fig. 6(a) also shows three stress–strain curves from continuum models, with different values of fracture energy G_f, where the discrete fracturing has not been activated. As expected, the lowest value of G_f, corresponding to the expected value for the quartzite, produces the most brittle response, with no regaining of the load after failure. Higher values of G_f results in deformation at almost constant stress levels prior to the final stress drop, which happens gradually. The model with fracturing activated also shows deformation at constant stress, but a much more sudden stress drop at the final failure. The stress levels and deformations agree well with the experimental data.

It is observed that the compressive fracture model, exhibiting explicit compressive–tensile coupling and the softening of the orthogonal tensile planes, produces the most brittle response, as expected.

In order to investigate the effect of including the compressive fracture model on the load deformation response and the fracture pattern, an analysis was performed with only tensile fracturing active i.e. by setting the compressive strength to a very high value. Fig. 7(e) shows the final fracture pattern when a purely tensile rotating crack model is adopted as the material model. It is apparent that only the axial cleavage crack is correctly recovered, with a complete absence of material degradation in the vicinity of the punch strip. This explains the excessive peak stress recovered (1300 MPa) and it is concluded that accurate numerical modelling of all punch or indenter processes requires the accurate modelling of material degradation obtained with the compressive fracture model in both tensile and compressive stress fields.

3.2. The plane strain and triaxial compression tests

Yumlu and Ozbay [8] tested $30 \times 30 \times 10$ mm prismatic specimens of coal, sandstone, norite and quartzite in plane strain and triaxial conditions, of which only the experiments on sandstone will be considered here. Fig. 8(a) shows the plane strain finite element model. For the plane strain experiments, the confining pressure was applied via a stiff system of discretely defined steel platens. The use of a threaded bolt across the sample (shown in the schematic diagram of Fig. 8(b) to provide confinement in the plane strain test) provides a constant stiffness and not a constant stress boundary condition. In the model (Fig. 8(a)), the confinement is applied with an initial applied displacement to the outside of the loading platen and the stiffness of the platen determines the subsequent system stiffness. Fig. 8(c) depicts the quarter symmetry triaxial finite element model. The hydraulic confinement of the triaxial test is modelled using a soft, applied stress condition as shown in Fig. 8(c). In both models, the ends of the specimen are loaded axially via prescribed velocities of $0.1 \, \text{m s}^{-1}$. A uniform mesh of linear plane strain elements of average dimension 0.5 mm and single point Gaussian quadrature is adopted. Material properties for the sandstone are defined by Yumlu and Ozbay [8] and the evolution of the cohesion, friction and dilation is given in Table 1. The Young's modulus is 28 GPa, the Poisson's ratio is 0.25, the density is 2800 kg m^{-3}, the tensile strength is 4 MPa and $G_f = 100 \, \text{J m}^{-2}$. The explicit Lagrangian contact algorithm is adopted for discrete contact, with the platen friction coefficient being 0.01 and the material friction coefficient is 1.3.

The best fit of the Mohr–Coulomb response to the triaxial test is used to determine the evolution of the cohesion, friction and dilation during the test. Fig. 9 shows the axial stress–strain curves obtained from the experiments on sandstone and the models. The experiments exhibit an initial non-linearity due to compaction of irregularities on the sample platen interface that has not been included in the models, and re-
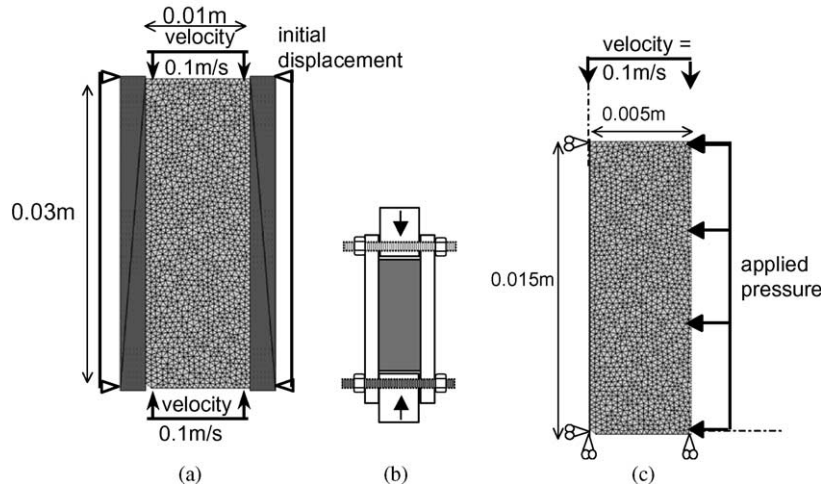
Fig. 8. (a) Plane strain finite element model, (b) schematic of plane strain experiment and (c) triaxial finite element model.
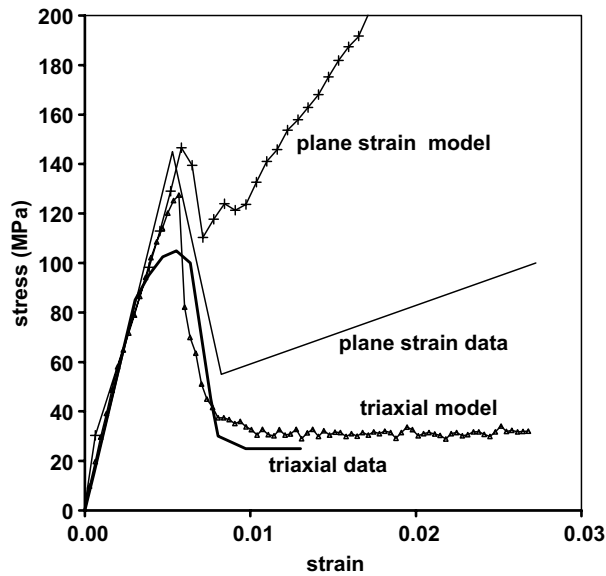

Fig. 9. Observed data (after Yumlu and Ozbay [8] with initial settling-in strains removed), and modelled compressive axial stress–strain curves for sandstone specimens tested under plane strain and triaxial conditions subject at a confining stresses of 3 MPa.

moved in the comparisons shown in Fig. 10. Considering the rest of the stress–strain response, the triaxial model shows the pre-failure plastic strain and low residual stress also observed in the experiments. The plane strain model shows a linear response with post-failure hardening. As shown in Fig. 10, the models are able to reproduce the correct strength increase with confinement and the strength difference between the triaxial and the plane strain models. Yumlu and Ozbay [8] observed that the plane strain constraint increases the peak strength and reduces pre-peak-non-linearity, and attribute this to different material responses for the different stress paths. However, as both models used the same material parameters, the
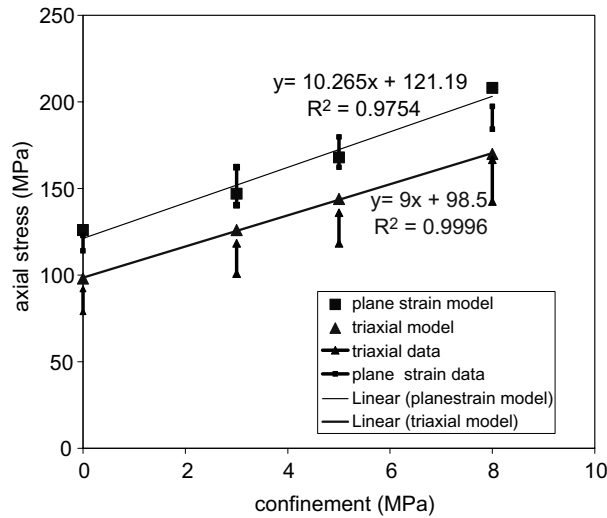
Fig. 10. The triaxial and plane strain principal stresses at failure, for the data [8] and models.

modelling indicates that the increased strength and residual hardening are not due to material properties, but are a response to the stiffer loading system in the plane strain test.

The evolution of the discrete fracture pattern post-localisation of material failure in plane strain is shown in Fig. 11a. The final pattern compares well with the observed failure shown in Fig. 12b. The constraint of inter-element fracturing does not permit the resolution of exactly vertical en-echelon fractures. The localisation occurs within one element width as expected for the crack band model, but would need to be refined to exactly match the observed fracture zone width. The localisation of failure in the triaxial models is similar to those of the plane strain example, as also noted for the experiments [8].

3.3. The borehole breakout

The fracture distribution around circular cavities has been widely observed in the literature and well documented by Hoek and Brown [48], Carter et al. [49,50], Sellers and Klerck [51], Lac du Bonnet granite
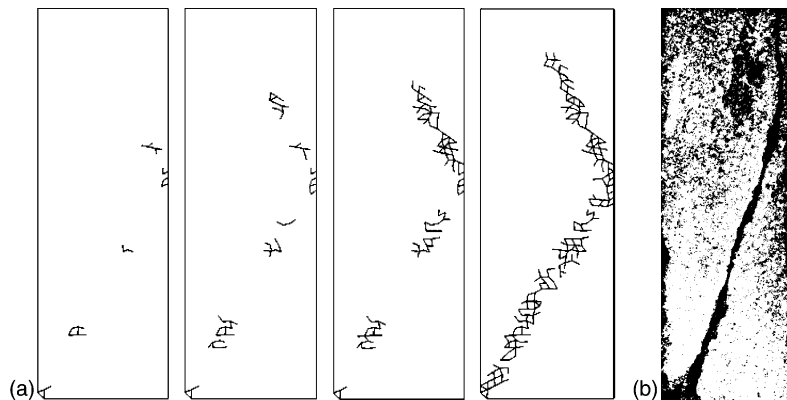
Fig. 11. (a) The evolution of discrete fracture in the localised failure zone, obtained using the compressive fracture model in plane strain and (b) the failure observed in the experiment.
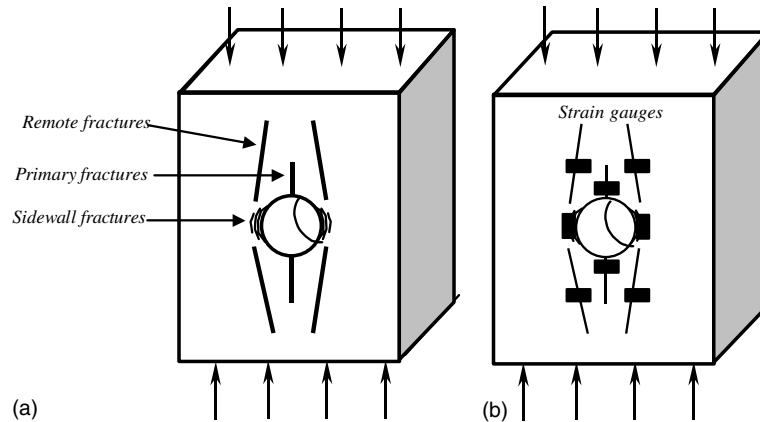
Fig. 12. (a) Primary, remote and sidewall fracture distribution around a circular cavity in uniaxial compression. (b) The location of strain gauges to indicate the initiation of different fracture types, after Carter [56].

tested by Lee and Haimson [52] or Berea sandstone tested by Ewy and Cook [53] and Zheng et al. [54] amongst many others. Fig. 12(a) shows the location of the so-called primary, remote and sidewall (borehole breakout) fractures around a circular cavity loaded in uniaxial compression [50]. The primary fractures initiate first from the tensile stress concentrations at the crown and invert of the circular cavity and propagate away from the cavity parallel to the direction of applied loading. The remote fractures form next, as shown in Fig. 12(a), initiating approximately adjacent to the termination of the primary fractures and at some distance from the circular cavity. These remote fractures are associated with the redistribution of tensile stress by the primary fractures and propagate away from and towards the cavity sidewalls. The four possible remote fractures do not generally initiate simultaneously and occasionally not all four fractures appear [50]. The third type of fracture is the sidewall fracture or borehole breakout that initiates with the compressive failure of the cavity sidewalls. The global failure mechanism observed in experimental specimens is generally due to the link up of the remote and sidewall fractures.

The mechanisms of borehole breakout in weak sedimentary rock, such as Cardova cream limestone considered by Haimson and Song [55] as well as the stronger and more brittle Lac du Bonnet granite tested by Lee and Haimson [51] were successfully modelled by Klerck [24]. The change in the fracture pattern surrounding borehole breakouts in Elsburg quartzite due to the presence of interfaces was also successfully simulated [51]. In this paper, the uniaxial compression tests performed by Carter and coworkers [50,56] on specimens of Tyndall limestone (Tyndallstone) are modelled. The aim of the numerical investigation is to demonstrate that the proposed compressive fracture model is able to recover the correct evolution of the primary, remote and sidewall fractures and exhibit the observed size effect. To the authors' knowledge this has not yet been achieved in the literature and would constitute a significant contribution to the study. Circular hole diameters ranging between 3.2 and 62 mm, were used to investigate the effect of hole size on fracture initiation around circular underground openings. All the blocks were 89 mm thick. Specimens were cut and polished into prismatic rectangular shapes with central circular holes and loaded via steel platens with teflon inserts. Strain gauges were positioned, as shown in Fig. 12(b), to indicate the initiation of primary, remote and sidewall fractures.

Numerical plane strain models of specimens tested by Carter et al. [50], with radii (R) of 6.4, 16.3 and 25 mm are illustrated in Fig. 13. Material properties for the limestone are deduced by matching the results of a single element triaxial test simulation with the triaxial data presented by Carter [56] and Carter et al. [50], and the evolution of the cohesion, friction and dilation is given in Table 1. The Young's modulus is 21 GPa,
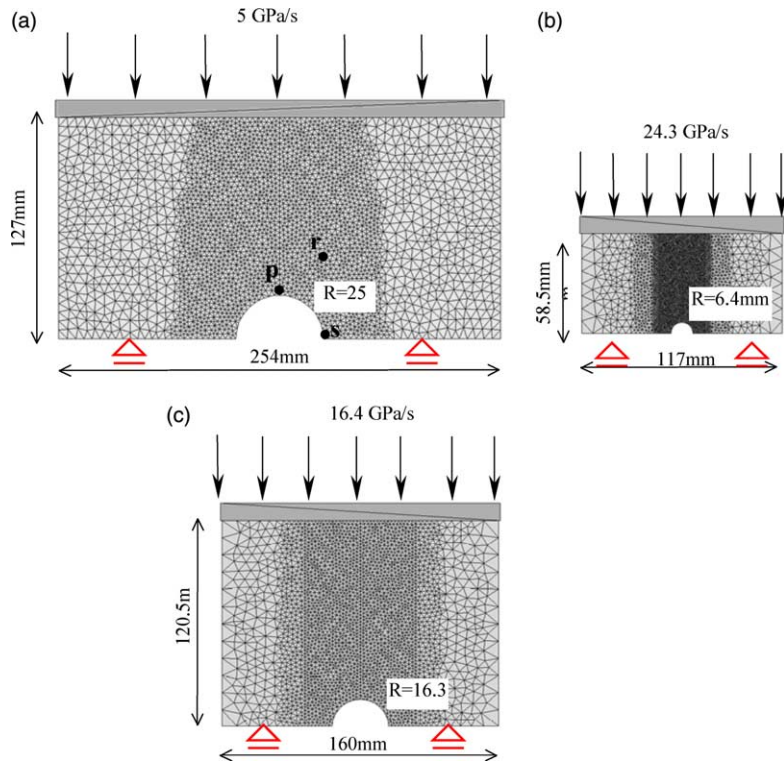
Fig. 13. The finite element models of the uniaxial loading of Tyndall limestone rectangular prisms with centrally located circular holes of radii (a) 25 mm (black dots mark positions of numerical "strain gauges"), (b) 6.4 mm and (c) 16.3 mm.

the Poisson's ratio is 0.3, the density is 2000 $kg\,m^{-3}$, the tensile strength is 1.5 MPa and $G_f = 9\,J\,m^{-2}$. The platen friction coefficient being 0.05 and the material friction coefficient is 0.58. Symmetry of the experimental system is invoked for convenience in the finite element models proposed in Fig. 13. Uniaxial stress loading is applied via discrete steel platens.

The results obtained using the compressive fracture model are shown in Fig. 14 for the specimen with radius $R = 25$ mm. Fig. 14 shows the evolution of the discrete numerical fracture pattern for the distinct stages of primary, remote and sidewall fracture. Clearly demonstrated is the lengthening of the remote fractures towards and away from the borehole walls, leading ultimately to the complete failure of the
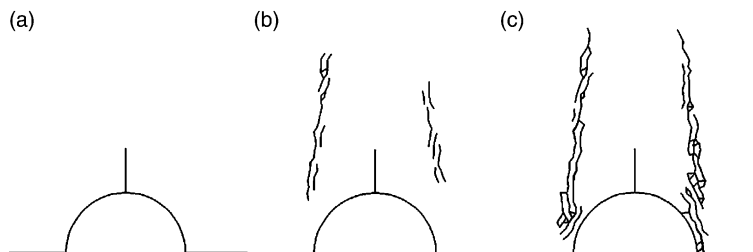

Fig. 14. Evolution of discrete fractures in borehole breakout model immediately after the stages of (a) primary initiation, (b) remote initiation and (c) sidewall initiation as indicated in Fig. 15.

specimen. The correspondence of the numerical response to the physical response observed by Carter and coworkers [49,50,56] is excellent.

The size effect of the initiation stresses of primary, remote and sidewall fractures around circular cavities has been widely observed in the literature, including Carter et al. [50], Lee and Haimson [52], Lajtai [57], Martin et al. [58], Martin [59]. The general trend is a decrease in fracture initiation stress with increasing cavity size and is of great importance in that physical experimental modelling is usually aimed at applications of a significantly larger scale. No single theory has yet been able to account for the observed size effect, although limited success has been achieved by Ewy and Cook [60] using fracture mechanics theory, Gonano [61] using a critical strain energy model, Lajtai [57] using stress averaging techniques and Santarelli and Brown [62] using pressure dependence of the elastic modulus. In order to assess whether the compressive fracture model is able to recover the physically observed size effect it is necessary to determine the stresses at which the different fractures initiate. This is achieved by monitoring the principal stresses in elements in the region of the primary, remote and sidewall fractures. The relevant element positions are marked in Fig. 13a. Initiation of the primary and remote fractures is indicated by a change in curvature of the axial stress versus the most extensional principal strain curve, while sidewall fracture is indicated by a change in the curvature of the axial stress versus the most compressive principal strain curve, as shown in Fig. 15. This method of indicating the initiation of fracture approximates the physical strain gauges used by Carter and coworkers [50,56]. The stresses agree well with the relevant experimental values. The observed strains are larger than the modelled strains. However, the monitoring of the stress and strain at individual element Gauss points is a local indicator, whereas the physical strain gauges are effectively non-local indicators. Also, the Tyndall Limestone is reported to have a significantly lower modulus in tension [56] which could account for the higher observed strains, as a single modulus is used for compression and tension in this analysis. In this experiment, the non-uniform stress state results in different parts of the model experiencing post-peak softening although the overall load–deformation response is hardening. The softened parts occur when cracks form and cause additional deformation. The good correspondence of the modelled and observed crack initiation stress levels and the resulting change in shape of the overall stress–strain curves at three separate points in the model as shown in Fig. 16, indicates that the model is correctly predicting the post-peak stress redistribution in the sample.

The experimental and numerical initiation stresses for primary, remote and sidewall fractures are plotted with respect to the hole radii in Fig. 16. Fracture initiation stresses are observed to decrease with increasing
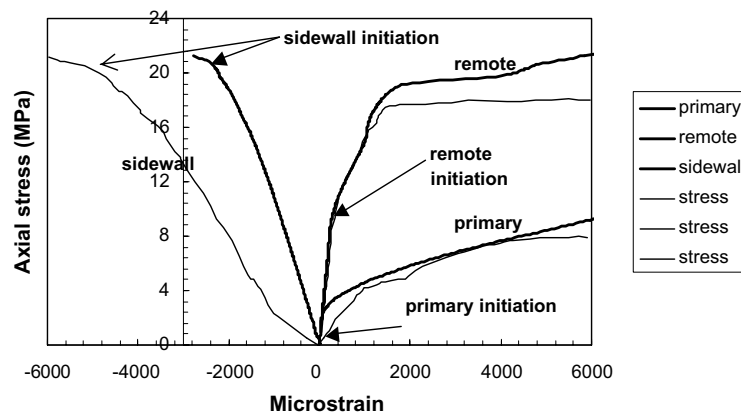

Fig. 15. Experimental (light lines) and numerical (dark lines) stress–strain response indicating initiation of primary (point p in Fig. 13), remote (point r in Fig. 13) and sidewall (point s in Fig. 13) fractures for $R = 25$ mm model.
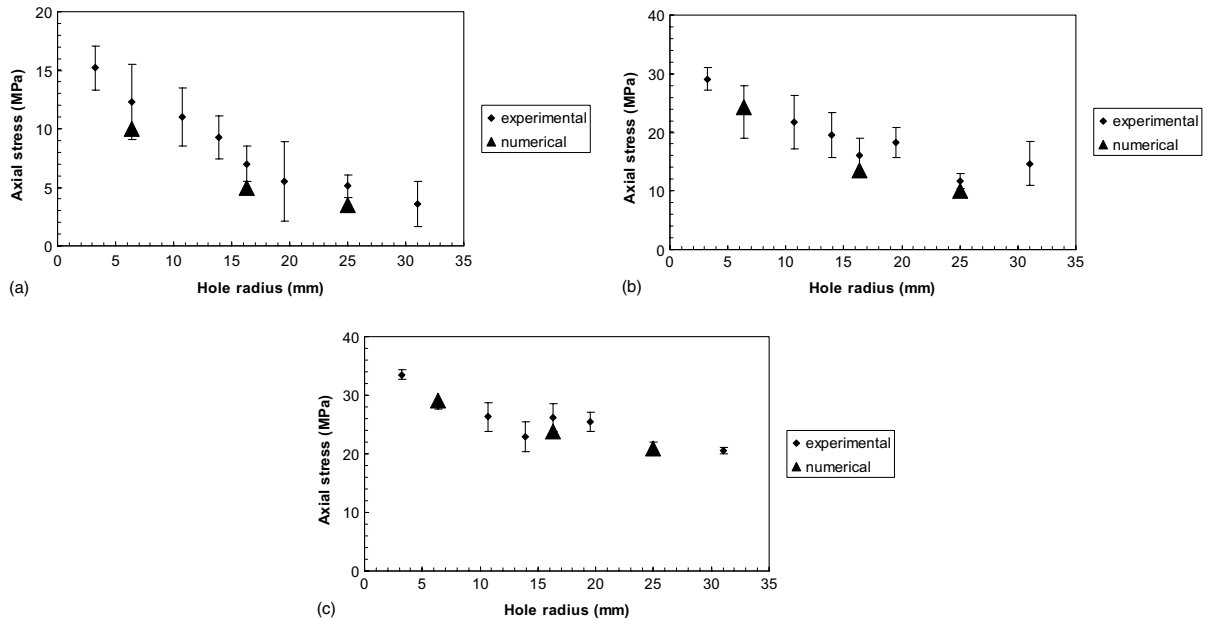
Fig. 16. The variation of fracture initiation stress with hole radius. (a) Primary, (b) remote and (c) sidewall for modelled results and data after Carter [56].

hole size and appear to approach different asymptotes for large cavity sizes. The numerical results obtained using the compressive fracture model appear to closely approximate the observed size effect. This is certainly understandable with respect to the primary and remote fractures that initiate in purely tensile stress fields, as the crack band model is effectively invoked with a response normalised by the material fracture energy. However, the compressive failure model is purely local and yet still appears to recover the physically observed size effect. This may be due to the fact that failure is not being localised into a single band of elements, but in finite regions determined by the geometry. Another more likely explanation is that the correct size effect response of the primary and remote fracture initiation offsets the compressive mode sidewall fracture initiation.

4. Conclusions

A method for modelling discrete fracture in geomaterials under tensile and compressive stress fields has been developed. The method is based on modifications to an explicit discrete element/finite element code. The model considers a failure envelope consisting of the Mohr–Coulomb failure surface in compression and three independent anisotropic rotating crack models in tension. To model fracture in the extension mechanism observed in compressive stress fields, the plastic strain induced by compressive failure is coupled to anisotropic rotating crack models. Once the tensile strength has been depleted, discrete fractures are inserted into the finite element mesh. An explicit Lagrangian contact algorithm is used to enforce non-penetration of the newly created fracture surfaces.

The model is applied to triaxial and plane strain tests as well as punch tests and borehole breakouts. These models exhibit fracturing in a range of stress states, sometimes with different modes in a single sample. The model is able to quantitatively predict the stresses at the initiation of fracturing, the defor-

mations associated with fracturing and the appropriate load–displacement response of the structure. The evolution of discrete fracturing is predicted and the fracture patterns are very similar to those observed in the experiments. Future work will concentrate on three-dimensional models to supplement the two-dimensional applications presented here.

References

[1] D.K. Hallbauer, H. Wagner, N.G.W. Cook, Some observations concerning the microscopic and mechanical behaviour of quartzite specimens in stiff, triaxial compression tests, Int. J. Mech. Min. Sci. Geomech. Abstr. 10 (1973) 713–726.
[2] P. Tapponnier, W.F. Brace, Development of stress-induced microcracks in westerly granite, Int. J. Mech. Min. Sci. Geomech. Abstr. 13 (1976) 103–112.
[3] J.A. Franklin, Triaxial strength of rock materials, Rock Mech. 13 (3) (1971) 86–98.
[4] W. Janach, Failure of granite under compression, Int. J. Rock Mech. Sci. Geomech. 14 (1977) 209–215.
[5] K. Mogi, Some precise measurements of fracture strength of rocks under uniform compressive stress, Rock Mech. Engrg. Geol. 4 (4) (1966) 41–55.
[6] K. Mogi, Effect of the intermediate principal stress on rock failure, J. Geophys. Res. 72 (20) (1967) 5117–5131.
[7] K. Mogi, Fracture and flow of rocks, in: A.R. Ritsema (Ed.), The Upper Mantle, Tectonophysics, vol. 13 (1–4), 1971, pp. 541–568.
[8] M. Yumlu, M.U. Ozbay, A study of the behaviour of brittle rocks under plane strain and triaxial loading conditions, Int. J. Rock Mech. Min. Sci. Geomech. Abstr. 32 (7) (1995) 725–733.
[9] E. Hoek, Z.T. Bieniawski, Brittle fracture propagation in rock under compression, Int. J. Fract. 1 (1965) 137–155.
[10] W.F. Brace, B.W. Paulding, C. Scholz, Dilatancy in the fracture of crystalline rocks, J.Geophys. Res. 71 (16) (1966) 3939–3953.
[11] E.Z. Wang, N.G. Shrive, Brittle fracture in compression: mechanisms, models and criteria, Engrg. Fract. Mech. 52 (6) (1995) 1107–1126.
[12] J. Ryder, CSIR Rock Engineering Textbook, C.S.I.R. (Miningtek), Johannesburg, South Africa, 1999.
[13] A.A. Griffith, Theory of rupture, 1st International Congress Appl. Mech., Delft, 1924, p. 55.
[14] W.F. Brace, E.G. Bombolakis, A note on brittle crack growth in compression, J. Geophys. Res. 68 (12) (1963) 3709.
[15] A.V. Dyskin, L.N. Germanovich, H. Joer, J.S. Krasinski, K.K. Lee, J.-C. Roegiers, E. Sahouryeh, K.B. Ustinov, Some results on three-dimensional crack propagation in compression, in: H.P. Rossmanith (Ed.), Mechanics of Jointed and Faulted Rock, Balkema, Rotterdam, 1995, pp. 91–96. ISBN 90-5410-5410.
[16] E.G. Bombolakis, Photoelastic investigation of brittle crack growth within a field of uniaxial compression, Tectonophysics 1 (4) (1964) 343–351.
[17] H. Horii, S. Nemat-Nasser, Compression induced microcrack growth in brittle solids: axial splitting and shear failure, J. Geophys. Res. 90 (B4) (1985) 3105–3125.
[18] E. Sahouryeh, A.V. Dyskin, The mechanism of 3-D crack growth in uniaxial compression: the role of non-singular stresses, Int. J. Rock Mech. Min. Sci. 34 (3–4), 1997, Paper No. 071.
[19] C.H. Scholz, Microfracturing and the inelastic deformation of rock in compression, J. Geophys. Res. 73 (4) (1968) 1417–1432.
[20] T. Engelder, Joints and shear fractures in rock, in: B.K. Atkinson (Ed.), Fracture Mechanics of Rock, Academic Press Inc, 1987.
[21] W.D. Ortlepp, Rock fracture and rockbursts an illustrative study, The South African Institute of Mining and Metallurgy, Johannesburg, SA, 1997. ISBN 1-874832-67-6.
[22] E. Sellers, F. Scheele, Prediction of anisotropic damage in experiments simulating mining excavations in Witwatersrand Quartzite blocks, Int. J. Rock Mech. Min. Sci. 33 (7) (1996) 659–670.
[23] A. Munjiza, D.R.J. Owen, N. Bićanić, A combined finite-discrete element method in transient dynamics of fracturing solids, Engrg. Comput. 12 (1995) 145–174.
[24] P. Klerck, The finite element modelling of discrete fracture in quasi-brittle materials. Ph.D. Thesis. University of Wales, Swansea, 2000.
[25] R. De Borst, Numerical aspects of cohesive-zone models, Eng. Frac. Mech. V 70 (2003) 1743–1757.
[26] P.H. Feenstra, Computational aspects of biaxial stress in plain and reinforced concrete, Ph.D., Delft University, 1993.
[27] J. Yu, A contact interaction framework for numerical simulation of multi-body problems and aspects of damage and fracture for brittle materials, Ph.D. dissertation, University of Wales, Swansea, 1999.
[28] T. Belytschko, An overview of semidiscretisation and time integration procedures, in: T. Belytschko, T.J.R. Hughes (Eds.), Computational methods for transient analysis, vol. 1, Elsevier Sci. Publ., 1983, pp. 1–65.
[29] E.A. De Souza Neto, D. Perić, D.R.J. Owen, Continuum modelling and numerical simulation of material damage at finite strain, Arch. Comput. Meth. Engrg. 5 (November) (1998) 311–384.
[30] L. Szabó, M. Balla, Comparison of some stress rates, Int. J. Solids Struct. 25 (3) (1989) 279–297.
[31] J. Bonet, R.D. Wood, Nonlinear Continuum Mechanics for Finite Element Analysis, Cambridge University Press, 1997.

[32] W.T. Koiter, Stress–strain relations, uniqueness and variational theorems for elasticplastic materials with a singular yield surface, Quart. Appl. Math. 11 (3) (1953) 350–354.

[33] R. De Borst, P. Nauta, Non-orthogonal cracks in a smeared finite element model, Engrg. Comput. 2 (1985) 35–46.

[34] Z.P. Bažant, J. Planas, Fracture and Size Effect in Concrete and Other Quasibrittle Materials, CRC Press LLC, 1998.

[35] Z.P. Bažant, B.-H. Oh, Crack band theory for fracture of concrete, Mater. Struct. 16 (1983) 155–177.

[36] K.J. Willam, E. Pramonno, S. Sture, Fundamental issues of smeared crack models, in: S.P. Shah, S.E. Schwartz (Eds.), Proc. SEM/RILEM Int Conf. on Fracture of Concrete and Rock, Springer Verlag, New York, Houston, 1989, pp. 142–157.

[37] J.G. Rots, R. De Borst, Analysis of mixed-mode fracture in concrete, J. Engrg. Mech. 113 (11) (1987) 1739–1758.

[38] Z.P. Bažant, L. Cedolin, Blunt crack band propagation in finite element analysis, J. Engrg. Mech. (ASCE) (105) (1979) 297–315.

[39] G.I. Barenblatt, The mathematical theory of equilibrium of cracks in brittle fracture, Adv. Appl. Mech. 7 (1962) 55–129.

[40] D.S. Dugdale, Yielding of steel sheets containing slits, J. Mech. Phys. Solids 8 (1960) 100–108.

[41] A. Hillerborg, M. Modéer, P.-E. Petersson, Analysis of crack formation and crack growth in concrete by means of fracture mechanics and finite elements, Cem. Concr. Res. 6 (1976) 773–782.

[42] J.C. Simo, J.G. Kennedy, S. Govindjee, Non-smooth multisurface plasticity and viscoplasticity. Loading/unloading conditions and numerical algorithms, Int. J. Numer. Methods Engrg. 26 (1988) 2161–2185.

[43] D. Perić, D.R.J. Owen, Computational model for 3-D contact problems with friction based on the penalty method, Int. J. Numer. Methods Engrg. 35 (1992) 1289–1309.

[44] D. Perić, E.A. De Souza Neto, A new computational model for Tresca plasticity at finite strains with an optimal parameterisation in the principal space, Comput. Methods Appl. Mech. Engrg. (171) (1999) 463–489.

[45] N.J. Carpenter, R.L. Taylor, M.G. Katona, Lagrange constraints for transient finite element surface contact, Int. J. Numer. Methods Engrg. 32 (1991) 103–128.

[46] Z. Zhong, L. Nilsson, Lagrange multiplier approach for evaluation of friction in explicit finite-element analysis, Comm. Numer. Methods Engrg. 10 (1994) 249–255.

[47] T. Dede, Fracture onset and propagation in layered media, M.Sc. dissertation, University of the Witwaterstrand, Johannesburg, South Africa, 1997.

[48] E. Hoek, E.T. Brown, Underground Excavations in Rock, Inst. of Mining and Metallurgy, London, 1980.

[49] B.J. Carter, E.Z. Lajtai, A. Petukhov, Primary and remote fracture around underground cavities, Int. J. Numer. Anal. Meth. Geomech. 15 (1991) 21–40.

[50] B.J. Carter, E.Z. Lajtai, Y. Yuan, Tensile fracture from circular cavities loaded in compression, Int. J. Fract. (57) (1992) 221–236.

[51] E.J. Sellers, P.A. Klerck, Modelling of the effect of discontinuities on the extent of the fracture zone surrounding deep tunnels under pressure, Tunnelling Underground Space Technol. 15 (2001) 463–469.

[52] M. Lee, B. Haimson, Laboratory study of borehole breakouts in Lac du Bonnet granite: a case of extensile failure mechanism, Int. J. Mech. Min. Sci. Geomech. Abstr. 30 (7) (1993) 1039–1045.

[53] R.T. Ewy, N.G.W. Cook, Deformation and fracture around cylindrical openings in rock—II. Initiation, growth and interaction of fractures, Int. J. Mech. Min. Sci. Geomech. Abstr. 27 (5) (1990) 409–427.

[54] Z. Zheng, J. Kemeny, N.G.W. Cook, Analysis of borehole breakouts, J. Geophys. Res. 94 (B6) (1989) 7171–7182.

[55] B. Haimson, I. Song, Laboratory study of borehole breakouts in cordova cream: a case of shear failure mechanism, Int. J. Mech. Min. Sci. Geomech. Abstr. 30 (7) (1993) 1047–1056.

[56] B.J. Carter, Size and stress gradient effects on fracture around cavities, Rock Mech. Rock Engrg. 25 (3) (1992) 167–186.

[57] E.Z. Lajtai, Effect of tensile stress gradient on brittle fracture initiation, Int. J. Rock Mech. Min. Sci. 9 (1972) 569–578.

[58] C.D. Martin, J.B. Martino, E.J. Dzik, Comparison of borehole breakouts from laboratory and field tests, Eurock '94, Balkema, Rotterdam, 1994, pp. 183–190. ISBN 90-5410-502-X.

[59] C.D. Martin, Seventeenth Canadian Geotechnical Colloquium: the effect of cohesion loss and stress path on brittle rock strength, Can. Geotech. J. (34) (1997) 698–725.

[60] R.T. Ewy, N.G.W. Cook, Deformation and fracture around cylindrical openings in rock—I. Observations and analysis of deformations, Int. J. Mech. Min. Sci. Geomech. Abstr. 27 (5) (1990) 387–407.

[61] L.P. Gonano, Stress gradient and size effect phenomena in brittle materials, Ph.D. dissertation, James Cook University, Townsville, Australia, 1974.

[62] F.J. Santarelli, E.T. Brown, Failure of three sedimentary rocks in triaxial and hollow cylinder compression tests, Int. J. Rock Mech. Min. Sci. Geomech. Abstr. 26 (1989) 401–413.